

**Supplementary Information for**  
**Modulation of assembly fashion among metal-organic**  
**frameworks for enantioselective epoxide activation**

Jun Guo,<sup>\*a,b</sup> Xiaomin Xue,<sup>a</sup> Fangfang Li,<sup>a</sup> Youcong Xing,<sup>b</sup> Yanmin Song,<sup>c</sup> Chang Long,<sup>d</sup> Tingting Zhao,<sup>a</sup> Yi Liu,<sup>\*a,e</sup> and Zhiyong Tang<sup>\*d</sup>

<sup>a</sup> State Key Laboratory of Separation Membranes and Membrane Processes, School of Chemistry, Tiangong University, Tianjin 300387, China.

<sup>b</sup> Institute of Scientific and Technical Research, Tiangong University, Tianjin 300387, China.

<sup>c</sup> Cosychem Technology (Tianjin) Co., Ltd., Tianjin 300457, China.

<sup>d</sup> CAS Key Laboratory of Nanosystem and Hierarchical Fabrication, CAS Center for Excellence in Nanoscience, National Center for Nanoscience and Technology, Beijing 100190, China.

<sup>e</sup> School of Chemical and Environmental Engineering, Wuhan Polytechnic University, Wuhan 430023, China.

Corresponding email: [junguo@tiangong.edu.cn](mailto:junguo@tiangong.edu.cn); [yiliu@whu.edu.cn](mailto:yiliu@whu.edu.cn);

[zytang@nanoctr.cn](mailto:zytang@nanoctr.cn)

## Contents

<b>Part S1. Chemicals and Reagents</b>	<b>Page S3</b>
<b>Part S2. Synthesis Methods</b>	<b>Page S4</b>
<b>Part S3. Calculation Methods</b>	<b>Page S6</b>
<b>Part S4. Characterizations</b>	<b>Page S7</b>
<b>Part S5. The Enantioselective Alcoholysis of Epoxides</b>	<b>Page S8</b>
<b>Part S6. Supplemented Figures and Tables</b>	<b>Page S9</b>
<b>Part S7. References</b>	<b>Page S24</b>

## Part S1. Chemicals and Reagents

Anhydrous zirconium chloride ( $\text{ZrCl}_4$ , 98%), zirconium oxychloride octahydrate ( $\text{ZrOCl}_2 \cdot 8\text{H}_2\text{O}$ , 99.9%), anhydrous formic acid (98%), *N,N*-dimethylformamide (DMF, 99.5%), racemic styrene oxide (97%), (*R*)-styrene oxide (97%, optical purity: 97% ee) and (*S*)-styrene oxide (97%, optical purity: 97% ee) were bought from Beijing Innochem Science & Technology Co., Ltd. Zirconium acetate (Zr content: 15.0-16.0%), terephthalic acid ( $\text{H}_2\text{BDC}$ , 99%), *N*-methylacridone (NMA, 98%) and acetic acid (99.7%) were purchased from Shanghai Aladdin Bio-Chem Technology Co., Ltd. Acetone (99.5%), methanol (MeOH, analytical grade), acetonitrile ( $\text{CH}_3\text{CN}$ , analytical grade) and ethanol (EtOH, analytical grade) were supplied by Tianjin Fengchuan Chemical Reagent Co., Ltd. The deionized (DI) water used in our experiments was obtained from the laboratory water purification system. All chemicals were used directly without further purification.

## Part S2. Synthesis Methods

### Synthesis of fcc-UiO-66 MOF

The **fcc-UiO-66** MOF was synthesized by using the acetic acid-modulated solvothermal method.<sup>1</sup> In detail, anhydrous zirconium chloride  $ZrCl_4$  (0.06 g, 0.17 mmol) and  $H_2BDC$  (0.06 g, 0.15 mmol) were dissolved in 15.0 mL of DMF. 1.5 mL of acetic acid was then added as the modulator for engineering linker defects. After sonication for 5 min, the homogeneous reaction mixture was transferred into a 25 mL polytetrafluoroethylene (PTFE)-lined autoclave and heated at a 120 °C oven for 24 h. After reaction, the product was collected by centrifugation (8400 rpm for 3 min) and washed with DMF for 3 times followed by ethanol for 3 times. Finally, white **fcc-UiO-66** powders were obtained after being dried at a 60 °C oven overnight.

### Synthesis of hcp-UiO-66 MOF.

The **hcp-UiO-66** MOF was synthesized by adopting the reported solvothermal method with slight modifications.<sup>2</sup> In specification, zirconium oxychloride octahydrate  $ZrOCl_2 \cdot 8H_2O$  (322.2 mg, 1 mmol) and  $H_2BDC$  (116.3 mg, 0.7 mmol) were added into a mixture composed of 10.0 mL of formic acid and 1.0 mL of water. The obtained mixture was sonicated for 5 min and then was transferred into a parapolyphenyl (PPL)-lined autoclave. The reaction was conducted at a 160 °C oven for 22 h. After reaction completion, the product was collected by centrifugation (8400 rpm for 3 min) and washed with DMF for 3 times followed by ethanol for 3 times. Finally, white **hcp-UiO-66** powders were obtained after being dried in a 60 °C oven overnight.

### Synthesis of hxl-CAU-26 MOF

The **hxl-CAU-26** MOF was synthesized by following the recently reported method.<sup>3</sup> In detail,  $H_2BDC$  (232.6 mg, 1.40 mmol) was dissolved in 20.0 mL of acetic acid and then 0.892 mL (~2 mmol) of zirconium acetate solution (15~16 wt% Zr) was added. The mixture was sonicated for 5 min and was transferred into a 25 mL PTFE-lined

autoclave. The reaction was conducted at a 160 °C oven for 22 h. After reaction completion, the product was collected by centrifugation (8400 rpm for 3 min) and wash with DMF for 3 times followed by ethanol for 3 times. Finally, white **hxl-CAU-26** powders were obtained after being dried in a 60 °C oven overnight.

### **The activation of MOF Catalysts**

60 mg of MOF powders were added into a 50 mL round-bottom flask charged with 20 mL of DMF. After ultrasonic treatment for 1 min, the mixture was stirred and heated at 100 °C for 12 h. The MOF powders were collected by centrifugation and 20 mL of fresh DMF was added for repeatedly heating. After two repeated cycles, the MOF powders were separated by centrifugation (9000 rpm for 3 min) and transferred to another round-bottom flask charged with 20 mL of MeOH. The mixture was stirred and heated at 80 °C for 12 h. Similarly, MOF powders were collected by centrifugation and 20 mL of fresh MeOH was added for repeatedly heating for twice. Furthermore, the separated MOF powders were solvent-exchanged with 20 mL of acetone at room temperature for 12 h. Finally, the activated MOF powders were obtained after drying them in a 60 °C oven overnight.

### **Part S3. Calculation Methods**

The charge distribution calculation was performed through the Dmol<sup>3</sup> Module integrated into the Material Studio software package.<sup>4</sup> The adopted model of metal node was withdrawn from the crystallographic structure of corresponding MOF. The electric charge density of metal node was calculated by the generalized gradient approximation (GGA)-Perdew-Burke-Ernzerhof (PBE) functional method with convergence tolerance set at the “fine” precision.<sup>5</sup>

## Part S4. Characterizations

Powder X-ray diffractions (PXRD) were recorded on a Bruker D8 ADVANCE diffractometer (Cu K $\alpha$ ,  $\lambda = 1.542 \text{ \AA}$ ) operating at 40 kV and 40 mA. Scanning electron microscope (SEM) measurements were carried out on a Hitachi S4800 scanning electron microscope at 5.0 kV. Transmission Electron Microscope (TEM) imaging and electron diffraction (ED) measurements were performed using a JEM-F200 microscope equipped with a field emission gun and operating at 200 kV. Fourier transform infrared (FT-IR) spectra were obtained on a Thermo Fisher Scientific Nicolet iS50 using the standard KBr disk method. Thermogravimetric analyses (TGA) were tested on a Netzsch TG 209 F3 Tarsus amid nitrogen flow of 1.0 mL/min and with a temperature range of 40 °C to 840 °C in a heating rate of 10 °C/min. The nitrogen adsorption tests were carried out on an ASAP 2460 analyzer (Micromeritics) with ultra-high pure nitrogen gas. The surface area was calculated from the adsorption data using the classical Brunauer-Emmett-Teller (BET) method. The pore size distributions were obtained from the adsorption branches using the density functional theory (DFT) method with the model of N<sub>2</sub>-DFT. Electron paramagnetic resonance (EPR) spectra were collected from a Bruker Elexsys 500 X-band EPR spectrometer at room temperature. The fluorescence (FL) spectra were recorded on a Gangdong F-320 fluorescence spectrophotometer. Catalytic product quantification was performed on a Nexis GC-2030 gas chromatography (GC) equipped with a chiral RtBDEXcst column and a flame ionization detector (FID).

### **Part S5. The Enantioselective Alcoholysis of Epoxides**

Firstly, 2 mg of MOF powders were dispersed into 5 mL of alcohol containing 28.5  $\mu\text{L}$  of epoxide substrate. The obtained mixture was transferred into a 15 mL glass vial and was further treated with ultrasonication for 30 seconds. The catalysis was initiated via placing the sealed reaction vial in the oil bath at a preset temperature. After a certain time of reaction, the MOF powders were separated by centrifugation (8000 rpm for 3 min). A small portion of the supernatant was sequentially taken for chiral GC analysis, which was installed with a chiral RtDEXcst column (30 m  $\times$  0.25 mm  $\times$  0.25  $\mu\text{m}$ ). The column temperature was set at 80  $^{\circ}\text{C}$  for 1 min, and ramping to 210  $^{\circ}\text{C}$  with a 5  $^{\circ}\text{C}/\text{min}$  rate, and maintained at 210  $^{\circ}\text{C}$  for 5 min. The injector temperature was set as 200  $^{\circ}\text{C}$  with a split ratio of 30:1. The FID temperature was set at 240  $^{\circ}\text{C}$  with the flow rate of  $\text{N}_2$  carrier of 1 mL/min.

## Part S6. Supplemented Figures and Tables.

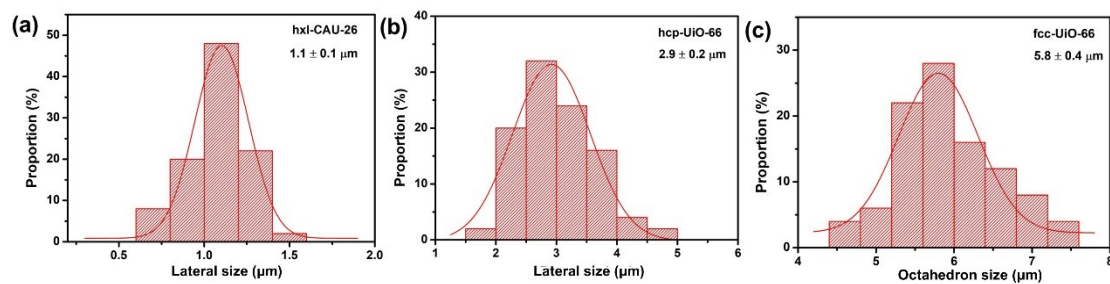


Figure S1. Lateral size of (a) **hxl-CAU-26** and (b) **hcp-UiO-66**. (c) Octahedron size of **fcc-UiO-66**.

According to statistical counting, **hxl-CAU-26** presents an average lateral size of  $1.1 \mu\text{m}$ , **hcp-UiO-66** presents an average lateral size of  $2.9 \mu\text{m}$  and **fcc-UiO-66** presents an average particle size of  $5.8 \mu\text{m}$ .

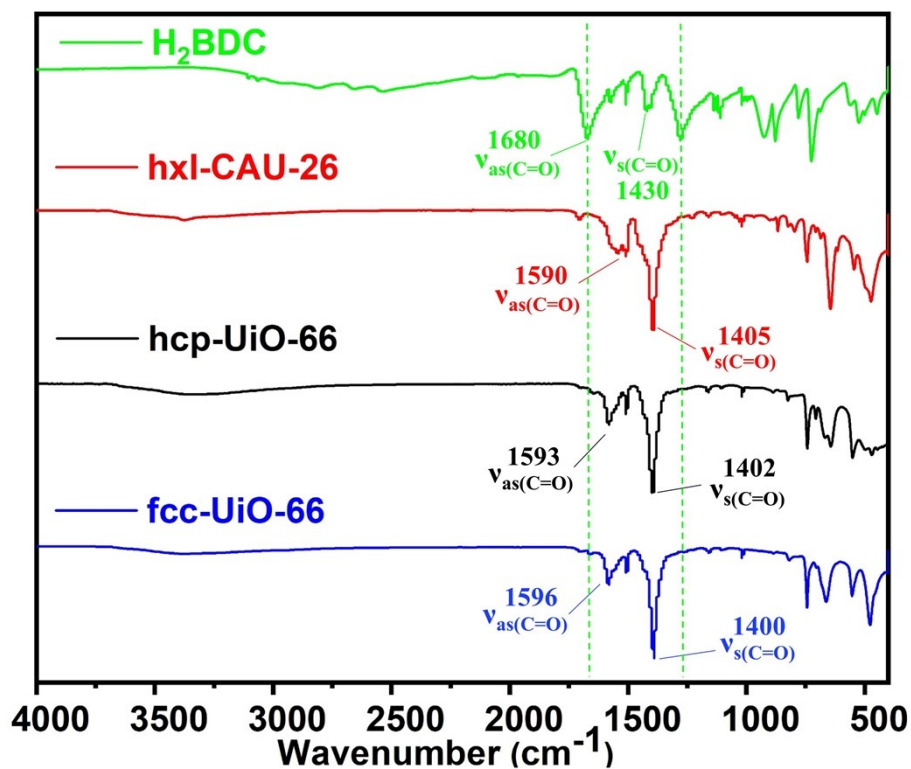


Figure S2. FT-IR spectra of **fcc-UiO-66** (blue curve), **hcp-UiO-66** (black curve), **hxl-CAU-26** (red curve) and **H<sub>2</sub>BDC** ligand (green curve).

Compared with free H<sub>2</sub>BDC ligand, the asymmetric stretching and symmetric stretching of the carboxylate group among MOFs all move towards lower wavenumbers due to coordination with metal sites. Moreover, the absence of characteristic peaks of H<sub>2</sub>BDC among each type of MOF samples also demonstrates the complete removal of residual H<sub>2</sub>BDC inside pores after activation.

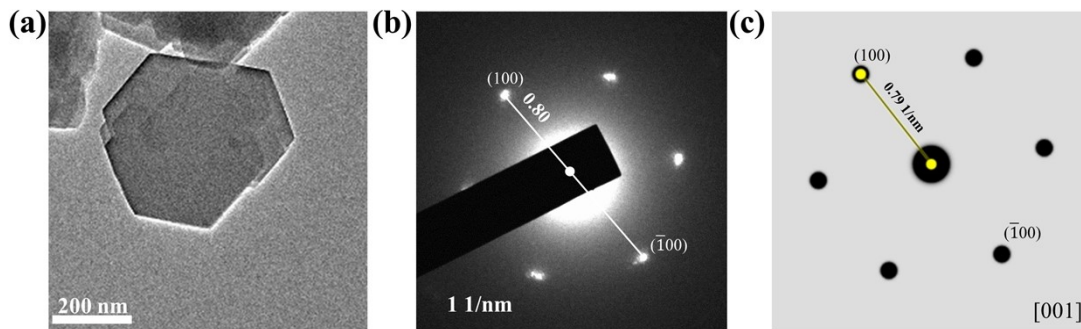


Figure S3. TEM image (a), observed electron diffraction (ED) (b) and simulated ED (c) of **hxl-CAU-26** nanosheets.

As shown in Figure S3a, **hxl-CAU-26** is of nanosheet morphology with hexagonal reciprocal lattices. The observed diffraction points (Figure S3b) are assigned to the  $d_{100}$  of 1.24 nm for **hxl-CAU-26**, in line with the simulated result (Figure S3c) with a theoretical  $d_{100}$  of 1.26 nm.

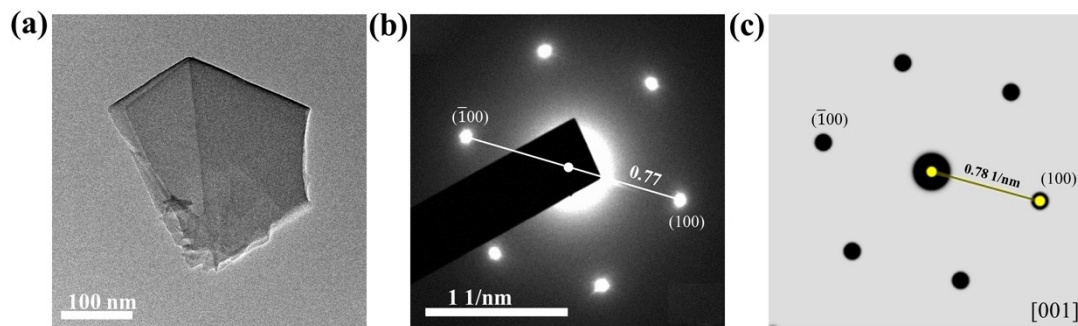


Figure S4. TEM image (a), observed electron diffraction (ED) (b) and simulated ED (c) of **hcp-UiO-66** nanosheets.

Similarly, as shown in Figure S4a, **hcp-UiO-66** is of nanosheet morphology with hexagonal reciprocal lattices. The observed diffraction point (Figure S4b) are assigned to the  $d_{100}$  of 1.29 nm for **hcp-UiO-66**, in line with the simulated result (Figure S4c) with a theoretical  $d_{100}$  of 1.28 nm.

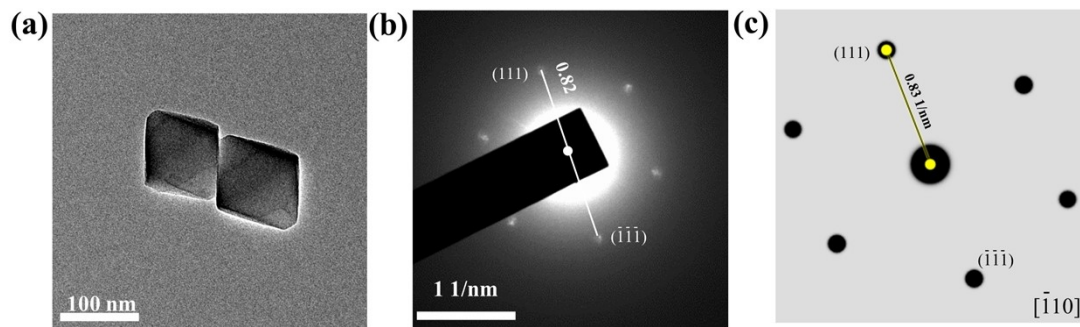


Figure S5. TEM image (a), observed electron diffraction (ED) (b) and simulated ED (c) of **fcc-UiO-66** nanosheets.

Distinctively, **fcc-UiO-66** shows octahedral morphology in Figure S5a. The observed diffraction point (Figure S5b) of **fcc-UiO-66** is assigned to the  $d_{111}$  of 1.22 nm, which is consistent with the theoretical value of 1.20 nm (Figure S5c).

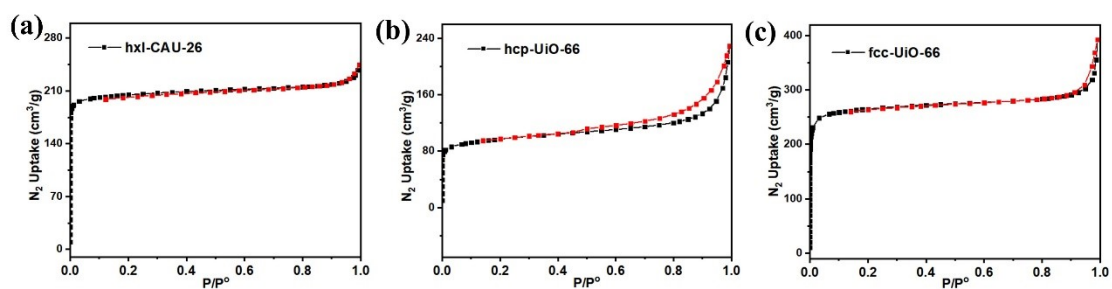


Figure S6. The nitrogen isotherm of (a) **hxl-CAU-26**, (b) **hcp-UiO-66**, (c) **fcc-UiO-66** at 77 K.

As shown in Figure S3, the obtained  $N_2$  adsorption/desorption curves all show type I isotherms. The BET specific surface areas calculated from adsorption branches are  $674.1 \text{ m}^2/\text{g}$ ,  $327.1 \text{ m}^2/\text{g}$  and  $876.5 \text{ m}^2/\text{g}$  for **hxl-CAU-26**, **hcp-UiO-66** and **fcc-UiO-66**, respectively.

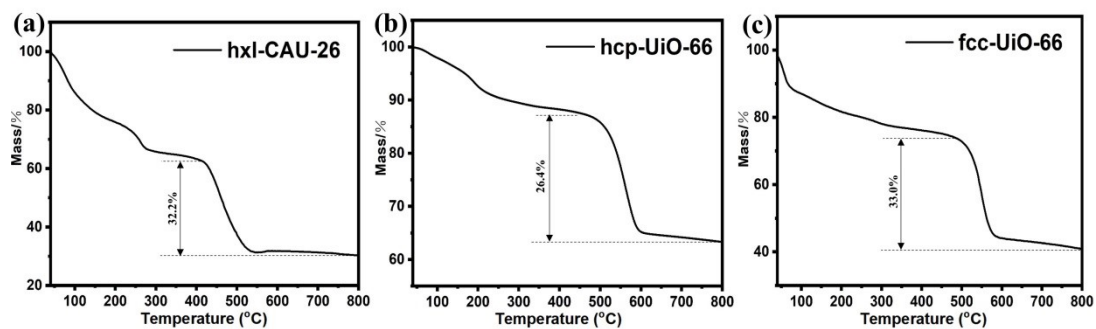


Figure S7. TGA result of (a) **hxl-CAU-26**, (b) **hcp-UiO-66** and (c) **fcc-UiO-66**.

According to TGA results, corresponding linker loss for each type of MOF is obtained and is used to calculate the linker defect number listed in the following Table S1.

Table S1. Linker defect assessment of **hcp-UiO-66**, **fcc-UiO-66** and **hxl-CAU-26**.

MOF	Obtained BDC Loss	Theoretical BDC Loss	Theoretical BDC No. Per Node	Obtained BDC No. Per Node	BDC Defect No. Per Node
<b>hcp-UiO-66</b>	26.4%	50.3%	18 <sup>a</sup>	9.4	8.6
<b>fcc-UiO-66</b>	33.0%	59.4%	12	6.6	5.4
<b>hxl-CAU-26</b>	32.2%	32.3%	6	6.0	6.0 <sup>b</sup>

<sup>a</sup> The metal node among **hcp-UiO-66** is considered as the Zr<sub>6</sub>O<sub>4</sub> dimer [Zr<sub>12</sub>O<sub>8</sub>(μ<sub>3</sub>-OH)<sub>8</sub>(μ<sub>2</sub>-OH)<sub>6</sub>] bridged by μ<sub>2</sub>-OH groups.

<sup>b</sup> According to the **hxl-CAU-26** formula [Zr<sub>6</sub>O<sub>4</sub>(BDC)<sub>6</sub>(CH<sub>3</sub>COO)<sub>4</sub>], the metal node has six defects occupied by acetates.

As for **hcp-UiO-66** and **fcc-UiO-66**, the obtained linker loss are obviously lower than corresponding theoretical percentage based on their crystallographic formula, indicating abundant exists of linker defects. Moreover, the obtained BDC number per node can be estimated:

$$\text{Obtained BDC No. Per Node} = \text{Theoretical BDC No. Per Node} \times \frac{\text{Obtained BDC Loss}}{\text{Theoretical BDC Loss}}$$

Hence, the defect number per node can be further calculated and shown in the following Table S1. However, the obtained BDC loss of **hxl-CAU-26** is in good line with the theoretical one, meaning the free of additional linker missing. Hence, its linker defect per node is considered as 6 acetate modulators according to the crystallographic formula of [Zr<sub>6</sub>O<sub>4</sub>(BDC)<sub>3</sub>(CH<sub>3</sub>COO)<sub>6</sub>].

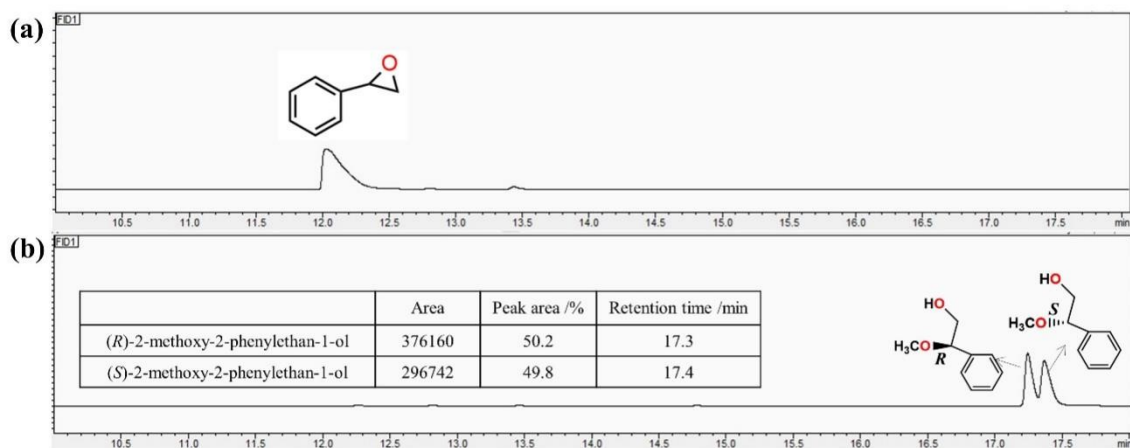


Figure S8. GC trace of (a) styrene oxide substrate, and (b) racemic 2-methoxy-2-phenylethan-1-ol.

The absolute configuration of 2-methoxy-2-phenylethan-1-ol enantiomer is assigned by referencing the reported literature.<sup>6</sup>

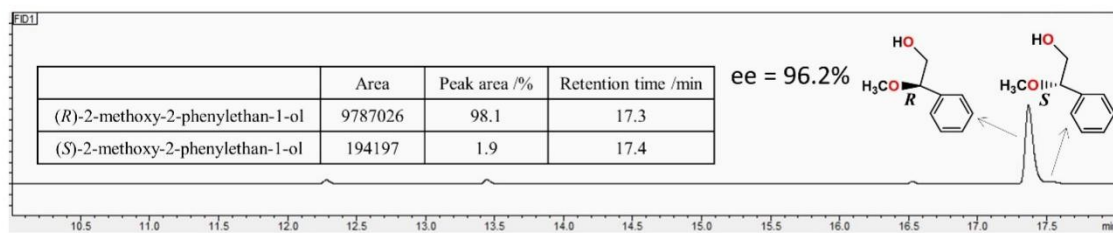


Figure S9. GC trace of the enantioselective methanolysis of (*S*)-styrene oxide catalyzed by **hcp-UiO-66** at 30 °C.

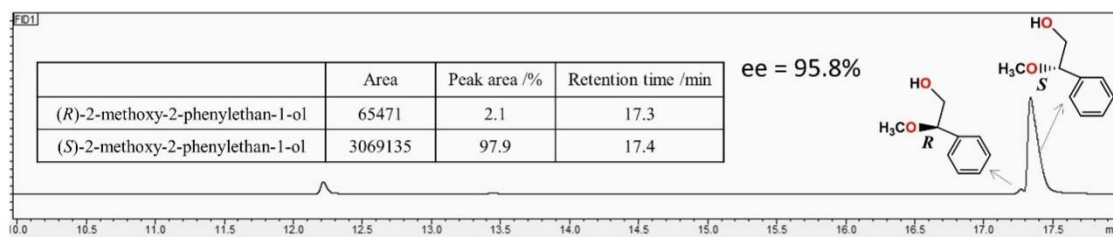


Figure S10. GC trace of the enantioselective methanolysis of (*R*)-styrene oxide catalyzed by **hcp-UiO-66** at 30 °C.

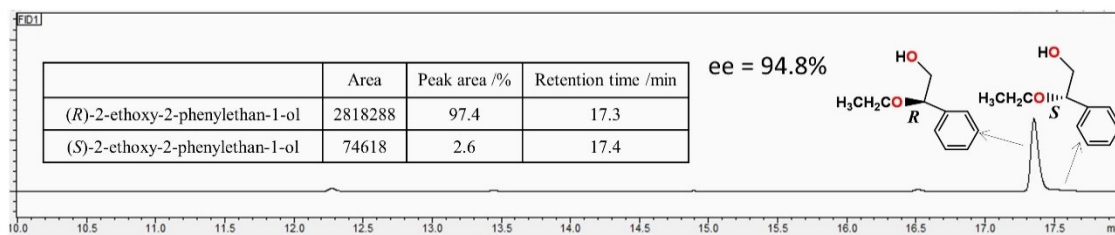


Figure S11. GC trace of the enantioselective ethanolic ring-opening of (*S*)-styrene oxide catalyzed by **hcp-UiO-66** at 60 °C.

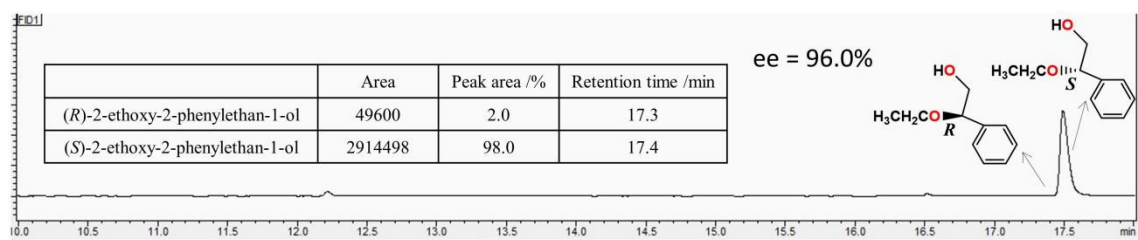


Figure S12. GC trace of the enantioselective ethanolic ring-opening of *(R)*-styrene oxide catalyzed by **hcp-UiO-66** at 60 °C.

Table S2. Comparison of methanolysis of (*S*)-styrene oxide catalyzed by different MOF catalysts and the homogeneous catalyst of ZrCl<sub>4</sub> under the same reaction temperature and time.

Entry	Catalyst	<i>T</i> /°C	<i>t</i> /h	Con./%
1	<b>hcp-UiO-66</b>	30	4	99.9
2	<b>fcc-UiO-66</b>	30	4	11.0
3	<b>hxl-CAU-26</b>	30	4	16.4
4	<b>ZrCl<sub>4</sub></b>	30	4	<1

In order to obtain the turnover frequency (TOF) based on per defect among three types of Zr-MOFs, reactions are therefore performed at otherwise same reaction conditions. As shown in Table S2, the calculated TOF per defect for **hcp-UiO-66**, **hxl-CAU-26** and **fcc-UiO-66** is 10.1 h<sup>-1</sup>, 1.2 h<sup>-1</sup>, and 1.0 h<sup>-1</sup>, respectively.

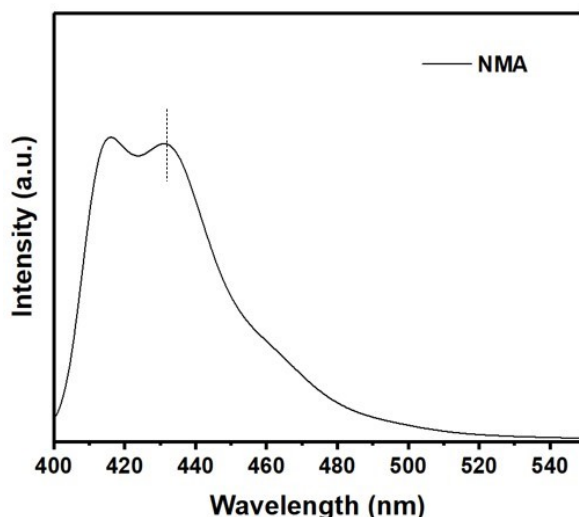


Figure S13. FL spectra of NMA dissolved in CH<sub>3</sub>CN. The excitation source is 413 nm. Hence, the strong background shoulder centered at 414 nm is caused by the excitation light. The FL peak centered at 433 nm is therefore ascribed to the emission of NMA.

The catalytic activation ability of metal sites among MOFs can be semi-quantitatively evaluated by referring to the NMA-based fluorescence protocol.<sup>7-10</sup> Specifically, NMA can bind to the open metal site among MOF and therefore result in a redshift of its emission wavelength due to the realignment of front orbitals. The emission energy change ( $\Delta h\nu$ ) of NMA correlates with the binding energy ( $\Delta E$ ) of metal site (equation 1):

$$\Delta h\nu = 0.383\Delta E - 0.13 \quad 1$$

In which,  $h$  is Planck constant ( $4.13566743 \times 10^{-15}$  eV·s),  $\Delta\nu$  is the frequency change of emission and can be derived from equation 2:

$$\Delta\nu = c/\lambda_{\text{NMA}} - c/\lambda_{\text{NMA-MOF}} \quad 2$$

In which,  $c$  ( $3.0 \times 10^8$  m/s) is the velocity of light,  $\lambda_{\text{NMA}}$  is the maximum emission wavelength of free NMA, and  $\lambda_{\text{NMA-MOF}}$  is the maximum emission wavelength of NMA binding to the metal site of MOF. The larger the value of  $\Delta E$ , namely, the stronger the activation ability of the metal site among MOF.

## Part S7. References

- [1] Wu, Y.; Wang, X.; Kirlikovali, K. O.; Gong, X.; Atilgan, A.; Ma, K.; Schweitzer, N. M.; Gianneschi, N. C.; Li, Z.; Zhang, X.; Farha, O. K., *Angew. Chem. Int. Ed.* 2022, **61**, e202117528.
- [2] Zhou, L.; Wang, S.; Chen, Y.; Serre, C., *Micropor. Mesopor. Mat.* 2019, **290**, 109674.
- [3] Leubner, S.; Zhao, H.; Van Velthoven, N.; Henrion, M.; Reinsch, H.; De Vos, D. E.; Kolb, U.; Stock, N., *Angew. Chem. Int. Ed.* 2019, **58**, 10995-11000.
- [4] Perdew, J. P.; Yue, W., *Phys. Rev. B* 1986, **33**, 8800-8802.
- [5] Li, K.; Li, N.; Yan, N.; Wang, T.; Zhang, Y.; Song, Q.; Li, H., *Appl. Surf. Sci.* 2020, **515**, 146028.
- [6] Beyzavi, H.; Klet, R. C.; Tussupbayev, S.; Borycz, J.; Vermeulen, N. A.; Cramer, C. J.; Stoddart, J. F.; Hupp, J. T.; Farha, O. K., *J. Am. Chem. Soc.* 2014, **136**, 15861-15864.
- [7] Ohkubo, K.; Menon, S. C.; Orita, A.; Otera, J.; Fukuzumi, S., *J. Org. Chem.* 2003, **68**, 4720-4726.
- [8] Ji, P.; Feng, X.; Oliveres, P.; Li, Z.; Murakami, A.; Wang, C.; Lin, W., *J. Am. Chem. Soc.* 2019, **141**, 14878-14888.
- [9] Ji, P.; Drake, T.; Murakami, A.; Oliveres, P.; Skone, J. H.; Lin, W., *J. Am. Chem. Soc.* 2018, **140**, 10553-10561.
- [10] Quan, Y.; Lan, G.; Shi, W.; Xu, Z.; Fan, Y.; You, E.; Jiang, X.; Wang, C.; Lin, W., *Angew. Chem. Int. Ed.* 2021, **60**, 3115-3120.